

Precision Positioning Using a Microfabricated Electrostatic Actuator

David A. Horsley, Naiyavudhi Wongkomet, Roberto Horowitz, and Albert P. Pisano
Berkeley Sensor & Actuator Center, 497 Cory Hall, University of California at Berkeley, CA 94720

Abstract — This paper presents a microfabricated actuator designed for high precision servo-positioning in a magnetic hard disk drive. The device is actuated using electrostatic force generated with parallel-plate capacitive electrodes. The displacement of these electrodes is measured using a dedicated capacitive sensing interface, allowing closed-loop control to be used to extend the servo bandwidth. Using the sensing electronics and a simple phase-lead compensator, a prototype device was used to actuate a 1.6 mg ceramic slider over a 1.2 kHz bandwidth. Using optical position measurements, the same actuator was used to achieve a 2.5 kHz bandwidth.

Index Terms — Actuator, disk drive, micro-electromechanical systems, position control.

I. INTRODUCTION

The magnetic hard disk drive continues to maintain a significantly lower cost per megabit in comparison to competing solid-state memory technology. One means of maintaining this advantage is through increasing the data storage density by reducing the size of each data bit, requiring increased accuracy in positioning the read/write heads over the disk. To this end, a dual-stage positioning mechanism has been proposed, using a conventional voice-coil motor (VCM) for coarse positioning and a high bandwidth secondary actuator for fine positioning [1]. The amount of disturbance attenuation achieved by this positioning mechanism is proportional to the square of the closed-loop bandwidth, which is defined as the -3 dB cross-over frequency of the closed-loop sensitivity transfer function from the disturbance input to the position error signal (PES) output. The implication of this relationship is that an order of magnitude improvement in track-misregistration (TMR) may be achieved by tripling the closed-loop bandwidth. As the present-day closed-loop bandwidth is approximately 600 Hz, the secondary actuator should be capable of a bandwidth of at least 2 kHz. Similarly, since the conventional, single-stage positioning system is currently used to achieve roughly 1 μm TMR, the secondary actuator must have a $\pm 1 \mu\text{m}$ displacement range. In terms of controller architecture, there are two potential types of dual-stage control systems. The first utilizes only the conventional position error signal (PES) to determine the position of the read/write heads with respect to the track center. For this approach to be successful, the actuator must behave in a predictable, and preferably linear, fashion, as the position of the actuator

must be estimated from a known model. The second scheme utilizes both the PES and a direct measurement of the displacement of the secondary actuator. To justify the cost of the additional signal processing electronics required by this approach, the electronics must provide sufficient measurement resolution to allow for very high precision positioning of the read/write heads.

This paper describes a microfabricated secondary actuator that measures 2.0 mm \times 2.2 mm \times 0.05 mm, occupying only slightly more area than the slider from a conventional disk drive. The actuator is designed to carry the slider and will itself be mounted on the VCM-actuated arm upon which the slider is usually attached. The advantage to this approach over competing designs is that the actuators are batch-fabricated for low cost, but are not expected to significantly effect either the head or suspension fabrication processes. The actuation dynamics are described by a simple, second-order linear model, and closed-loop control has been implemented using both optical and capacitive position measurement techniques. Moreover, nonlinear effects such as stiction or backlash are absent in these devices, so that the closed-loop positioning accuracy is determined by the resolution of the position measurement.

II. ACTUATOR DESIGN

The actuator, illustrated in Fig. 1, consists of a translating central shuttle which is anchored to fixed stator segments via a flexural suspension. In contrast to earlier rotational designs which had only a small surface for mounting the slider [2], the new design has a shuttle which is large enough to allow for easy assembly of the slider onto the actuator. Actuation is achieved by electrostatic force generated using capacitive electrodes which are mounted in opposing pairs between the shuttle and stator. The device is quad-symmetric, meaning that the upper stator segments are used to pull the shuttle in the positive x direction, while the lower segments are used to push the shuttle in the negative x direction. Electrostatic actuation has been selected for ease of fabrication, since the structural material need only be conductive, rather than ferromagnetic or piezoelectric. Because the disk-drive application requires high output force over a relatively small displacement range ($\pm 1 \mu\text{m}$), parallel plate capacitors have been selected rather than interdigitated (“comb-finger”) electrodes [3]. The main drawback to this configuration is that the electrostatic attraction between parallel-plate capacitors is a nonlinear function of the separation between the plates. However, assuming a nominal capacitive gap of g_0 and an electrode length of l_p , the ratio of the parallel-plate force to the interdigitated force is

Manuscript received April 16, 1998.

D.A. Horsley, present address: DiCon Fiberoptics, (510) 528-0427, Fax: (510) 528-1519, dhorsley@diconfiberoptics.com.

This work was supported in part by DARPA contract DABT 63-95-C-0028.

proportional to l_p/g_0 [4]. Since typical electrode lengths are over ten times greater than the capacitive gap, the parallel plate configuration enjoys an order of magnitude greater output force than an interdigitated design with the same area and capacitive gap.

It is well known that a voltage driven parallel plate has a stable actuation range of $\pm g_0/3$ [5]; at larger displacements the electrostatic force dominates over the restoring force from the suspension and the electrodes pull together. Due to the difficulty of isolating multiple stator electrodes, the design illustrated in Fig. 1 places the stator electrode from the $(n-1)$ -th shuttle/stator electrode pair at a distance αg_0 from the shuttle electrode from the n -th electrode pair. The result is that a "parasitic" capacitive gap is created, somewhat reducing the total output force and the stable operating range. In this case, there is no simple analytic solution for the maximum stable displacement; for a given value of α and g_0 this maximum displacement may be calculated numerically. For example, actuators were fabricated with $g_0 = 12 \mu\text{m}$ and $\alpha g_0 = 26 \mu\text{m}$, yielding a computed maximum stable displacement range of $3.7 \mu\text{m}$. To prevent the electrodes from exceeding this displacement and coming into contact due to a large external shock, fixed stoppers which are biased at the same potential as the shuttle are placed above and below the shuttle, limiting the

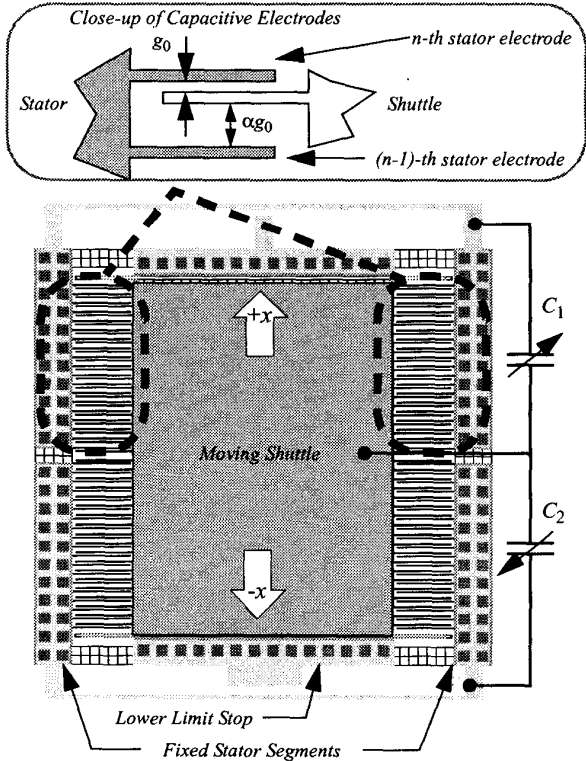


Fig. 1. Actuator layout. The upper stator segments (circled) serve to pull the shuttle in the $+x$ direction, while the symmetric lower stator electrodes push the shuttle in the $-x$ direction.

displacement to a maximum range of $\pm 4 \mu\text{m}$.

A. Electrostatic Actuation

As illustrated in Fig. 1, the actuator may be modeled as two variable capacitors, C_1 and C_2 , connected in series. Neglecting fringing fields, the capacitance between the shuttle and the upper stator segments is approximated by:

$$C_1(x) = C_f + N\epsilon_a A \left(\frac{1}{g_0 - x} + \frac{1}{\alpha g_0 + x} \right) \quad (1)$$

where C_f denotes the displacement independent capacitance (0.5 pF), N is the number of shuttle-stator capacitor pairs (38), ϵ_a is the permittivity of air (8.86 pF/m), A is the area of each capacitive plate (0.015 mm^2), while g_0 and αg_0 are the nominal capacitive gaps between the shuttle electrode and its two nearest stator electrodes ($12 \mu\text{m}$ and $26 \mu\text{m}$, respectively). Microfabrication allows symmetry between the upper and lower shuttle-stator capacitors, so that the lower shuttle-stator capacitance, C_2 , is given by $C_2(-x) = C_1(x)$.

The electrostatic attraction generated by applying a voltage, V , to a pair of capacitive electrodes is given by:

$$F(x, V) = \frac{1}{2} \left(\frac{\partial C}{\partial x} \right) V^2 \quad (2)$$

Considering the push-pull electrode configuration, the total electrostatic force is the sum of the force generated by the positive and negative stator halves, $F_T = F_1 + F_2$. Combining (1) and (2), for applied voltages V_1 and V_2 , these forces are given by:

$$F_1(x, V_1) = \frac{N\epsilon_a A}{2} \left(\frac{1}{(g_0 - x)^2} - \frac{1}{(\alpha g_0 + x)^2} \right) V_1^2 \quad (3)$$

$$F_2(x, V_2) = -\frac{N\epsilon_a A}{2} \left(\frac{1}{(g_0 + x)^2} - \frac{1}{(\alpha g_0 - x)^2} \right) V_2^2$$

Although the force described above is a nonlinear function of both applied voltage and displacement, increased linearity is achieved by using a dc bias voltage V_0 and a differential voltage v_c :

$$V_1 = V_0 + v_c \quad V_2 = V_0 - v_c \quad (4)$$

In this case, $F_2(x, v_c) = F_1(-x, -v_c)$, and antisymmetry implies that the even terms in the series expansion for the total electrostatic force will be cancelled, so that only odd powers remain. A linear approximation for this force is then given by the first-order Taylor-series expansion:

$$F_T(x, v_1) \approx k_e(V_0)x + k_v(V_0)v_c \quad (5)$$

where:

$$k_e(V_0) = \left. \frac{\partial F_T}{\partial x} \right|_{(0, V_0)} = \frac{2N\epsilon_a A}{g_0^3} \left(1 + \frac{1}{\alpha^3}\right) V_0^2$$

$$k_v(V_0) = \left. \frac{\partial F_T}{\partial v_1} \right|_{(0, V_0)} = \frac{2N\epsilon_a A}{g_0^2} \left(1 - \frac{1}{\alpha^2}\right) V_0$$
(6)

B. Actuation Dynamics

For small deflections, $x(t)$, the mechanical behavior of the actuator in response to an applied electrostatic force, $F_T(x, v_c)$, may be described by a mass-spring-damper model,

$$m\ddot{x}(t) + b\dot{x}(t) + k_m x(t) = F_T(x, v_c) \quad (7)$$

where m denotes the total mass of the slider and actuator, b is the damping coefficient, and k_m is the suspension spring constant. The damping coefficient accounts for the effect of viscous gas damping effects on the surface of this shuttle. Both squeeze-film [6] and slide-film [7] damping models were used to produce an estimate for this damping coefficient. The suspension spring constant, on the other hand, was estimated from linear beam theory [8].

Substituting the linearized electrostatic force from (5) into (7), the actuator equation of motion, yields a linear actuation model:

$$m\ddot{x}(t) + b\dot{x}(t) + (k_m - k_e(V_0))x(t) = k_v(V_0)v_c \quad (8)$$

Note that k_v represents a voltage-to-force gain, while the effect of k_e is that of a negative, electrostatic spring. This electrostatic spring term reflects the tendency for the parallel plates to pull together for sufficiently high voltage, which occurs when $k_e(V_0) \geq k_m$.

For a fixed bias voltage, V_0 , the Laplace transform of (8) is that of a simple second-order system,

$$\frac{X(s)}{V_c(s)} = \frac{k_v(V_0)}{ms^2 + bs + (k_m - k_e(V_0))} \quad (9)$$

Typical microfabricated actuators exhibit very lightly damped resonances, implying that if the resonant frequency is near the desired servo bandwidth, the settling performance will be poor. One approach is to design the actuator to have an extremely high resonance frequency so that the actuator dynamics will have negligible effect on the servo system performance. For this approach to succeed, the resonance frequency should be from five to ten times greater than the servo bandwidth. Alternatively, the actuator may be designed to have an open-loop resonant frequency which is well within the control bandwidth. Feedback is then used to provide the desired closed-loop resonant frequency and damping ratio. The advantage of the latter approach is quickly seen by noting that the dc gain of the actuator transfer function listed in (9) is:

$$A_0 = \left(\frac{m}{k_m - k_e(V_0)} \right) \left(\frac{k_v(V_0)}{m} \right) = \frac{1}{\omega_n^2} \left(\frac{k_v(V_0)}{m} \right) \quad (10)$$

Thus, for a fixed mass and bias voltage, an actuator which has a resonance that is within the control bandwidth will require one-hundred times lower input voltage to achieve the same displacement as an actuator with a resonant frequency which is ten times higher. For the disk-drive application, a CMOS charge-pump capable of producing 80 V from the 5 V bus voltage is planned. This suggests that the actuator must be capable of achieving a dc gain of at least 25 nm/V in order to produce the desired range of $\pm 1 \mu\text{m}$.

III. FABRICATION PROCESS

Actuators were fabricated using a modified version of the HexSil process first described in [9]. The advantage of this process is that it produces high aspect-ratio structures with heights of up to 200 μm using a molded, 4 μm thick, chemical-vapor deposited (CVD) polysilicon film. A simplified process flow chart is illustrated in Fig. 2. Molds are fabricated by etching deep trenches into standard (100) silicon wafers using deep reactive ion etching (DRIE). Since the depth of these trenches determines the height of the finished actuators, the mold DRIE is a critical process. Prototype molds were limited to 50 μm depths, but future devices will have doubled thickness and output force. Following the mold fabrication, the mold is filled with in-situ phosphorous doped polysilicon

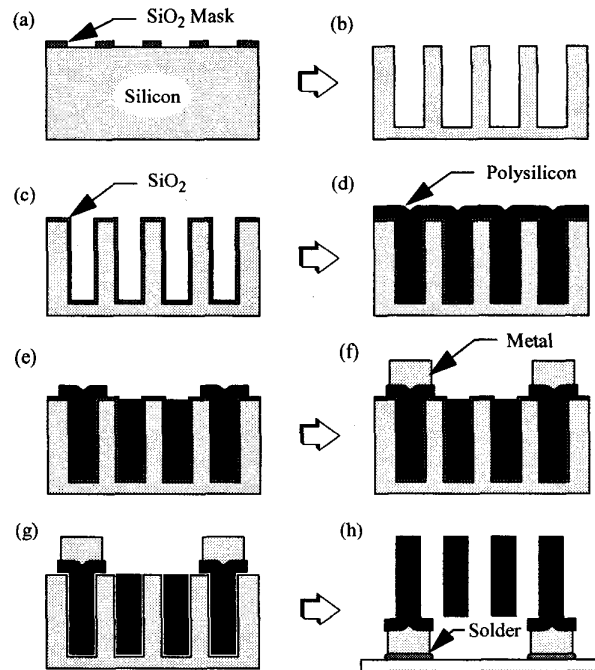


Fig. 2. Simplified HexSil process flow. A SiO_2 masking layer is deposited and patterned on a silicon wafer (a). DRIE is used to define deep trenches in this wafer, forming a mold (b). A sacrificial SiO_2 layer is deposited onto the mold (c), followed by a structural polysilicon layer (d). The polysilicon on the wafer surface is then patterned (e) and metallized (f). Following an HF etch to remove the SiO_2 , the finished actuator is released from the mold wafer and assembled onto a target substrate using a solder bond.

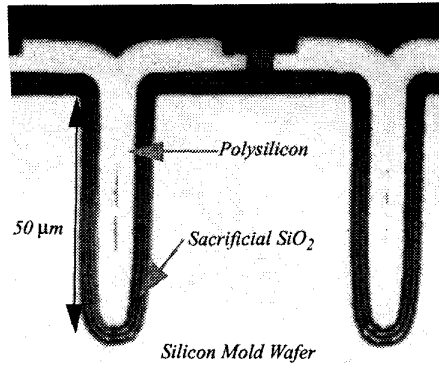


Fig. 3. Optical micrograph of filled mold trenches. Note that slight bowing of the mold trenches has resulted in voids in the polysilicon beams. Also, bright bands in the sacrificial layer are observed due to incomplete oxidation.

on top of a SiO_2 sacrificial layer, both deposited via CVD. To ensure conformality of the SiO_2 film it is formed by thermally oxidizing a conformal CVD polysilicon layer. The surface polysilicon is then patterned and metallized using conventional surface micromachining techniques. A cross-sectional optical micrograph of the filled trenches is shown in Fig. 3. Note that there are bright bands visible in the sacrificial layer due to incomplete oxidation of the polysilicon. The completed structures are released from the mold wafer by an etch in hydrofluoric acid (HF), which removes the sacrificial layer. The actuators are then assembled onto copper interconnect on a target substrate using a solder bump bonding process described in [10]. Due to the fact that the structural material is uniformly conductive, electrical isolation is achieved through the use of break-away or fusible beams as illustrated in Fig. 4. These beams are narrower than the adjoining beams, making them both mechanically weaker and more resistive than surrounding beams. A brief current pulse applied across these beams is sufficient to vaporize them.

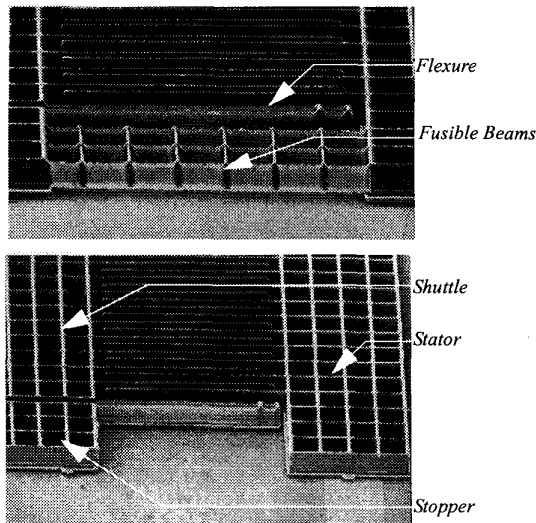


Fig. 4. Electrical isolation of assembled actuators. Top: fusible beams connecting the stopper and stator segments. Bottom: the same region after the application of a brief pulse of current.

IV. CLOSED-LOOP ACTUATION

For a second-order system, the closed-loop dc gain and the resonant frequency are related to their open-loop values by:

$$A_{cl}\omega_{n,cl}^2 = A_0\omega_n^2 = \text{GBW} \quad (11)$$

where GBW is a constant, analogous to the gain-bandwidth product used to describe first-order systems such as op-amps. Although slight increases in bandwidth may be obtained at the cost of diminished phase-margin, the actuation bandwidth is roughly proportional to the resonant frequency. Thus, feedback can be used to trade dc gain for bandwidth or vice-versa. However, (11) shows that in order to double the closed-loop bandwidth, the closed-loop dc gain must diminish by a factor of four. A simple control design technique is to choose a loop gain which yields the desired closed-loop bandwidth, then use the remaining controller parameters to achieve a specified phase-margin or damping ratio. The block-diagram of the control system is illustrated in Fig. 5.

A. Position Measurement Techniques

The actuator displacement is measured using the capacitive position sensing interface illustrated in Fig. 6. The custom sensing circuit utilizes a pseudo-differential switched-capacitor capacitive sensing scheme [11]. The differential signal path improves linearity and reduces power supply and noise coupling, while the switched-capacitor sensing scheme eliminates the need for large dc-setting resistors and provides flexibility in interfacing with the microactuator drive circuit. On-chip coupling capacitors shield the sensing electronics from the high-voltage drive signal, which is in the range of ± 40 V. The amplifier offset, $1/f$ noise, switch-charge injection, and kT/C sampling noise, which produce errors that are several orders of magnitude larger than the amplifier thermal noise floor, are removed by correlated double sampling (CDS). The concept of CDS is to remove relatively constant errors by performing two measurements and subtracting the results from each other. The measured capacitance-to-voltage sensitivity of the circuit was 0.7mV/fF , while the sensitivity of the actuator capacitance to displacements was $56\text{fF}/\mu\text{m}$. Combining these two numbers results in a displacement sensitivity of $39\text{mV}/\mu\text{m}$. To minimize the coupling of the driving signal into the sensing signal, the sensing frequency is chosen to be more than two orders of magnitude higher than the microactuator drive bandwidth, and the driving signal is held

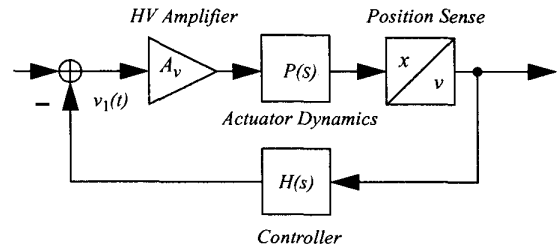


Fig. 5. Block-diagram of closed-loop control architecture.

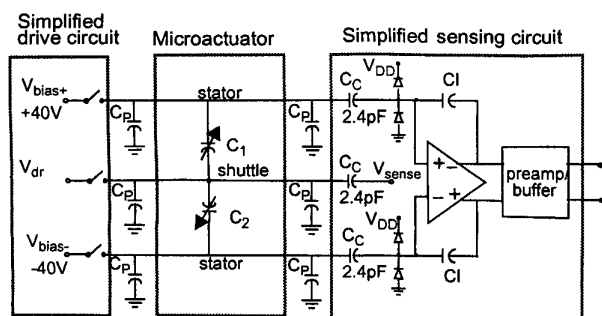


Fig. 6. Simplified circuit for capacitive sensing interface.



Fig. 7. Scanning electron micrograph of a 1.2 mm \times 1.0 mm \times 0.3 mm slider assembled onto the 2.2 mm \times 2.0 mm \times 0.05 mm actuator.

constant during the period in which the measurement is being performed. Unfortunately, this coupling, referred to as feedthrough, is not completely suppressed and the position sensing resolution is limited to approximately 20 nm. There are two limitations created by the feedthrough signal. Firstly, while the dc gain from input voltage to actuator displacement is attenuated by feedback, the feedthrough term is not. This fact implies that feedthrough accounts for a larger fraction of the measured signal as the feedback gain (and closed-loop bandwidth) is increased. Secondly, the feedthrough term adds additional phase lag to the measurement signal at higher frequencies, effectively limiting the maximum achievable bandwidth. For purposes of comparison, a laser doppler vibrometer (LDV) was also used for position measurements. The advantage of this device is that it allows measurement of both actuator position and velocity over a bandwidth of more than 50 kHz, with a position resolution of approximately 2 nm. The use of LDV measurements allowed the implementation of a very high closed-loop bandwidth, demonstrating the full positioning potential of the actuator.

V. EXPERIMENTAL RESULTS

The parameters of the open-loop actuation transfer function listed in (9) were identified by measuring the actuator frequency response using LDV measurements. A slider with a measured mass of 1.6 mg was bonded to an actuator, as shown in Fig. 7. Open-loop frequency response measurements taken before and after attaching the slider, presented in Fig. 8,

allowed the moving mass of the actuator to be estimated at $97 \pm 10 \mu\text{g}$. All remaining measurements were performed with the slider permanently affixed to the actuator. Measurements of the resonant frequency and dc gain at multiple bias voltages, illustrated in Fig. 9, allowed estimates for the suspension spring constant, k_m , as well as the electrostatic model parameters, k_v and k_e , to be produced. The values estimated from experimental data are listed along with theoretically estimated values in Table 1. In the table, m_a refers to the mass of the moving portion of the actuator with no attached slider. Two different actuator designs were fabricated which were identical except for the fact that one had a larger (and more massive) shuttle than the other. Good agreement is observed between the measured and theoretical values with the exception of the damping coefficient. This error is due to the fact that the theoretical damping model included only viscous gas damping and did not account for added damping due to series resistance between the input amplifier and the capacitive electrodes.

Following the open-loop system identification experiments, closed-loop control was implemented on the actuated slider using measurements from both the LDV and the capacitive sensing interface. Due to the fact that the actuator gain/resonant frequency product described in (11) was lower than the

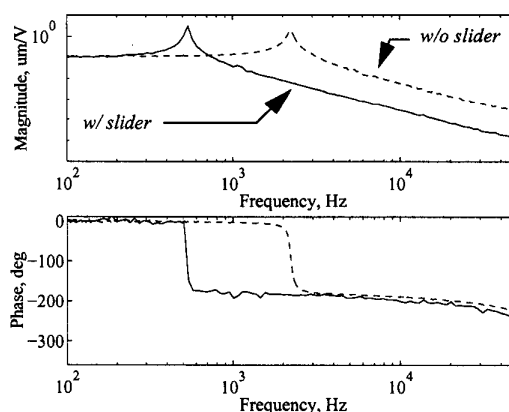


Fig. 8. Measured actuator frequency response with and without an attached pico-slider.

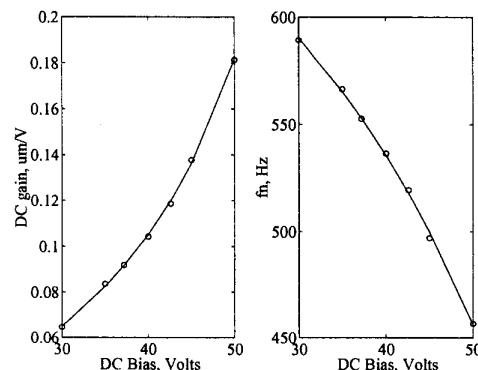


Fig. 9. Measured dc gain and resonance frequency (with attached slider) vs. bias voltage.

TABLE 1: ACTUATION MODEL PARAMETERS AT $V_0 = 40\text{V}$

	$m_a, \mu\text{g}$	$b, \mu\text{Ns/m}$	$k_m, \text{N/m}$	$k_e, \text{N/m}$	$k_v, \mu\text{N/V}$
Design #1, measured	97 ± 10	78 ± 12	29 ± 2	9.4 ± 0.6	2.0 ± 0.1
Design #1, theoretical	87	41	33	10.1	2.2
Design #2, measured	44 ± 5	58 ± 14	29 ± 2	9.4 ± 0.6	2.0 ± 0.1
Design #2, theoretical	46	33.5	33	10.1	2.2

desired value, the specified dc gain of 25 nm/V could not be achieved with a bandwidth greater than approximately 1.5 kHz . For this reason, both a high-bandwidth, low-gain design and a low-bandwidth, high-gain design were tested. Future devices with doubled thickness (and capacitance) will allow the desired gain to be achieved over the full 2 kHz bandwidth. Both proportional-derivative (PD) and phase-lead control designs were tested with similar performance results, the phase-lead approach having the advantage of simpler implementation [12]. In each case, the controller was designed using the second-order linear model described by (9). Using LDV measurements, a high-bandwidth PD control design was used to yield a closed-loop bandwidth and dc gain of 2.5 kHz and $0.01 \mu\text{m/V}$, respectively. The closed-loop response of this design to a $\pm 5 \text{ V}$, 500 Hz square wave is illustrated in Fig. 10. Note that the steady-state tracking error is approximately 2 nm , corresponding to the maximum resolution of the LDV position signal. Although the closed-loop response of this design settles to within 1% of the final value within $500 \mu\text{sec}$, it has the disadvantage of a dc gain of only 10 nm/V . Next, using the capacitive measurement electronics, a phase-lead controller was implemented, yielding a closed-loop bandwidth and dc gain of 1.2 kHz and 35 nm/V , respectively. Note that this controller was intentionally designed to have lower bandwidth than the PD control design; there is no fundamental performance limitation imposed by the phase-lead compensator approach. Using this controller, the closed-

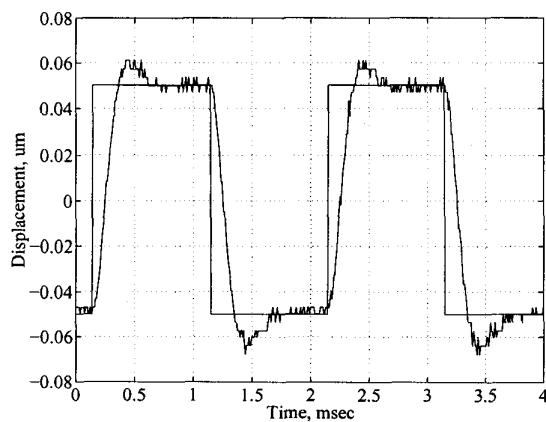


Fig. 10. Optically measured closed-loop response of the actuated slider to a $\pm 5 \text{ V}$, 500 Hz square-wave.

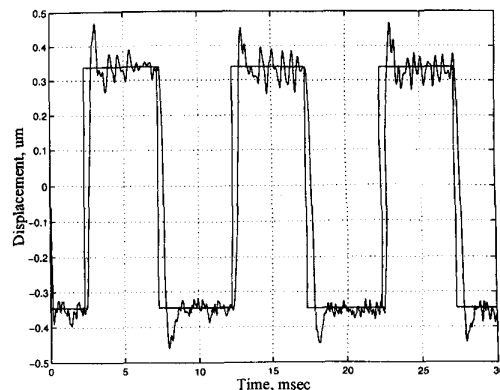


Fig. 11. Capacitively measured closed-loop response of the actuated slider to a 100 Hz square-wave.

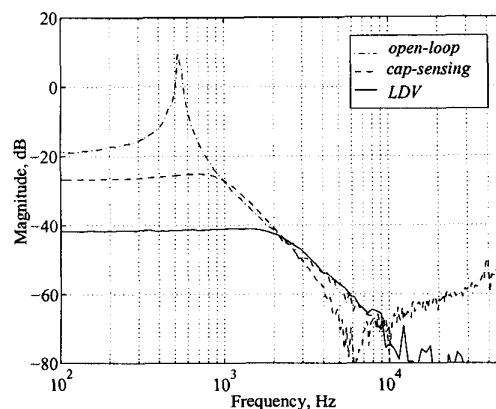


Fig. 12. Measured open- and closed-loop frequency response of the actuated slider.

loop response to a 100 Hz , $\pm 10 \text{ V}$ square-wave, measured using capacitive sensing, is plotted in Fig. 11. For purposes of comparison, the measured open and closed-loop transfer functions for both controller designs are shown in Fig. 12. Note that the higher bandwidth achieved using LDV measurements came at a cost of a four-fold reduction in dc gain, corresponding to a greatly reduced actuation range at $\pm 40 \text{ V}$. A summary of the closed-loop results is provided in Table 2.

VI. CONCLUSIONS

Closed-loop position control of a disk-drive slider has been demonstrated using a microfabricated actuator. A dedicated capacitive sensing interface was utilized to demonstrate a closed-loop bandwidth of 1.1 kHz , although reducing the dc gain by a factor of four allowed a bandwidth of over 2.4 kHz to be achieved using optical position measurements. The device was accurately modeled by a second-order linear system, and no higher order resonant modes were observed at frequencies below 51 kHz . Additionally, no measurable nonlinearities such as stiction or hysteresis were detected, allowing a 2 nm positioning accuracy to be demonstrated. Future devices which have a doubled thickness will allow a proportionate increase in dc gain and capacitive sensing resolution. These devices will then be capable of providing the desired gain of 25 nm/V over the full 2 kHz bandwidth.

TABLE 2: SUMMARY OF OPEN & CLOSED-LOOP RESULTS

	dc gain, $\mu\text{m/V}$	-3 dB BW, Hz	Phase Margin, Deg.	t_{settle} - msec.
Open-Loop	0.1	820	NA	100
LDV	0.01	2474	45	0.5
Cap. Sensing	0.035	1170	38	2.0

ACKNOWLEDGMENTS

The authors thank Chris Keller, Angad Singh, and Michael Cohn for their help with developing the actuator fabrication process, along with Stephen Williams of Quantum Corporation for providing the pico-sliders.

REFERENCES

1. L.-S. Fan, H.H. Ottesen, T.C. Reiley, R.W. Wood, "Magnetic Recording-Head Positioning at Very High Track Densities Using a Microactuator-Based, Two-Stage Servo System", *IEEE Trans. Ind. Electronics*, v 42, pp. 222-233, June 1995.
2. D.A. Horsley, A. Singh, R. Horowitz, A.P. Pisano, "Angular Micropositioner for Disk Drives," *Proc. 10th Intl. Conf. on MEMS (MEMS '97)*, Nagoya, Japan, pp. 454-459, 1997.
3. W.C. Tang, "Electrostatic Comb Drive for Resonant Sensor and Actuator Applications", Ph.D. Dissertation, University of California at Berkeley, May 1990.
4. T. Imamura, T. Koshikawa, M. Katayama, "Transverse Mode Electrostatic Microactuator for MEMS-Based HDD Slider," *Proc. 9th Int. Conf. on MEMS (MEMS '96)*, San Diego, CA, pp. 216-221, 1996.
5. J.I. Seeger, S.B. Crary, "Stabilization of Electrostatically Actuated Mechanical Devices," *Proc. Intl. Conf. on Solid-State Sensors and Actuators*, Chicago, IL, 16-19 June 1997, New York, NY, pp. 1133-1136 vol.2.
6. J.B. Starr, "Squeeze Film Damping in Solid State Accelerometers," *Proc. 1990 Solid-State Sensor and Actuator Workshop*, Hilton Head, SC, pp. 44-47, June 1990.
7. Y.H. Cho, B.M. Kwak, A.P. Pisano, R.T. Howe, "Slide Film Damping in Laterally Driven Microstructures", *Sensors and Actuators A*, 40, 1994, pp. 31-39.
8. R.J. Roark, W. C. Young, "Formulas for Stress and Strain", 5th ed, pp. 118-127.
9. C.G. Keller and M. Ferrari, "Milli-Scale Polysilicon Structures," *1994 Solid-State Sensor and Actuator Workshop*, Hilton Head, SC, pp.132-137.
10. A. Singh, D.A. Horsley, M.B. Cohn, A.P. Pisano, R.T. Howe, "Batch Transfer of Microstructures using Flip-Chip Solder Bump Bonding," *Transducers '97*, Chicago, IL, pp. 265-268.
11. N. Wongkomet, D.A. Horsley, B. Boser, "A Capacitive Position Sensing Circuit for Microactuators," to appear at *12th European Conf. on Solid-State Transducers*, Southampton, UK, Sept. 1998.
12. B.C. Kuo, *Automatic Control Systems*, 6th ed., New Jersey: Prentice Hall, 1991, pp. 669-691.